Strain gauge measurements on a full scale tidal turbine blade

Thomas Lake [a, *], Jack Hughes [a], Michael Togneri [a], Alison J. Williams [a], Penny Jeffcoate [b], Ralf Starzmann [c], Nicholas Kaufmann [c], Ian Masters [a]

[a] College of Engineering, Swansea University, Bay Campus, Fabian Way, Swansea, SA1 8EN, UK
[b] Sustainable Marine Energy, La Belle Esperance, The Shore, Edinburgh, UK
[c] SCHOTTEL HYDRO, Mainzer Straße 99, 56322, Spay/Rhine, Germany

ARTICLE INFO

ABSTRACT

The development of tidal energy converters, and particularly floating tidal energy converters, is an area of increased development in recent years. Testing of a floating tidal energy device over winter 2017/18 led to an opportunity to record and examine strain of a full scale composite turbine blade under operational conditions, with comparison of generating and parked behaviours. Comparison of the recorded data shows that blade strain correlates well with both torque and thrust over the averaging periods specified in IEC62600-200, although examination of frequency spectra generated from the strain data show that higher frequency fluctuations in strain are not necessarily detectable in the larger scale thrust and torque recordings with this particular measurement arrangement. The need for well synchronised clocks on recording systems is also highlighted, along with a cross-correlation method used to recover the alignment of data from different systems to allow comparison between them over periods of a similar order of magnitude to the clock skew between the systems.

1. Introduction and background

The development and deployment of floating tidal energy converters (FTECs) is an area which has seen increased activity in recent years, with a number of developers trialling and testing devices in the class. These devices have some potential advantages over bed mounted tidal energy devices, including the ability to be deployed using smaller vessels, easier access for operations and maintenance (O&M) purposes and reduced disruption to the seabed.

The sites at which devices are tested and deployed are highly energetic (by necessity - there needs to be enough energy present in the water flowing through the area to be extracted), with both spatial and temporal variations present, ranging from turbulent fluctuations [1–3] to larger bathymetry dependent flow features [4,5], vertical flow profiles and asymmetric flood/ebb flow speeds and direction [6,7]. These flow variations lead to fluctuations in the loads on the devices, which is then reflected in operational performance [8,9] as well as repeated load cycling that may lead to fatigue damage. Work in the wind sector suggests that typical wind

turbines are "fatigue critical" - parts are more likely to fail through fatigue than through over loading and need to be designed accordingly [10], and while loadings on tidal devices will be different (and are likely to be higher), it is likely that the survivability and reliability will also require careful consideration of the unsteady nature of the forces acting upon them [9,11].

In order to examine the loads acting on a tidal energy device, strain gauges and load cells are often mounted to or incorporated into the blades as in Refs. [9,12,13], blade root or mounting fixtures [14,15] and/or the supporting structures of the device under test [8,16–18]. These loads can then be compared to the turbine operating parameters, including rotation rate and generated power, and the upstream flow speed. The upstream flow speed can often be controlled in a lab environment, but must be measured during field testing. Depending on the environment, the upstream flow speed can be measured using a range of techniques, from optical particle image velocimetry (PIV) and laser doppler velocimetry (LDV) systems [14,19] to acoustic doppler velocimeter (ADV) [20–22] and acoustic doppler current profiler (ADP or ADCP) [1,3,9] devices. Not all of these are applicable in all environments, with PIV and LDV systems being primarily used in laboratory settings, ADCP devices being mainly used in large scale field environments and ADVs being used in both settings. The flow conditions and operating loads can then be compared in order to examine which conditions expose the

* Corresponding author.
E-mail address: t.lake@swansea.ac.uk (T. Lake).

device to greatest loads and fatigue risks.

The SURFTEC project (**Su**rvivability and **R**eliability of **F**loating **T**idal **E**nergy **C**onverters) at Swansea University has been investigating the behaviour of floating tidal energy converters alongside industry partners, particularly with respect to reliability and survivability impacts. This investigation has included a measurement campaign carried out with Sustainable Marine Energy (SME) on their PLAT-I device (shown in Fig. 1). PLAT-I is a floating tidal energy converter (FTEC), consisting of three floating hulls coupled with a cross-deck structure. This cross-deck structure supports four SCHOTTEL Instream Turbines (SITs), with each turbine mounted to a lifting structure referred to as an SDM (SIT Deployment Module). The turbines are three-bladed horizontal axis tidal stream turbines with passive-adaptive blades [5]. All four turbines are connected to a common direct current bus via individual inverters, and during these tests the energy generated by the turbine was dissipated into a load bank - an alternating current immersion heater mounted to the side of the platform [24].

Initial sea acceptance trials of PLAT-I were carried out between November 2017 and June 2018 south west of the Falls of Lora at Connel, Scotland (see Fig. 2). The site has a significant flood-ebb asymmetry, leading to generation on the ebb tides only. This is due to a jet formed by underwater overfalls formed as water flows out of Loch Etive through a shallow, narrow neck underneath Connel bridge. This leads to accelerated flows with substantial spatial variation in what is otherwise a calm and sheltered test location [5,25].

As part of these initial trials, a period of testing was arranged with additional instrumentation to allow the strain on a single blade to be recorded under operational and parked conditions. This work was carried out by personnel from Sustainable Marine Energy, Swansea University, SCHOTTEL Hydro and Epsilon Optics on the 2nd and 3rd of March 2018. Initially the testing had been planned to start on the 28th of February, but was delayed due to "unseasonably low temperatures and significant snowfall" [26], leading to delayed equipment delivery to site. This reduced the data collection period to 24 h, with approximately 18 h useable as detailed below.

The aim of this additional testing period was to allow the strains recorded on the instrumented blade to be compared to the other loads acting on the platform, and to explore any patterns in these variables or their correlations with the inflow velocity. The two ebb tides present in the recorded data allow difference in loads and behaviour with the turbines parked and generating to be compared. Selected variables from the recorded data are presented below as timeseries, with some additional comparisons against bins of inflow velocity based on the methods presented in the International Electrotechnical Commission (IEC) standard [27].

Frequency spectra have been generated from the recorded data in order to explore any frequency dependence in the recorded data, which may impact on the fatigue life of the platform or turbines.

The main contributions of this paper are to show that strain and thrust are well correlated on both two different averaging periods and that cross-correlation can be applied to re-align timeseries data where the timestamps on recorded data were insufficiently synchronised. These results are placed in context with flow and operational data collected concurrently during this test period.

2. Test design and setup

The test aimed to record the strain at three locations on a single full size blade concurrent with the operating and environmental conditions. The strain was measured at the surface of the blade using fibre Bragg grating type sensors bonded to the blade surface, and an interrogator in a waterproof housing fitted into the turbine hub. The strain sensors were located such that one was parallel with the longitudinal axis of the blade on the pressure face, another mounted parallel on the suction face of the blade and a third mounted at 45° on the pressure face to capture blade twist, as illustrated in Fig. 3. Note that the blade outline shown is illustrative and does not reflect the actual profile of the blades installed on the device. All three strain gauges were mounted at a radial distance of 600 mm from the rotor axis. This location was chosen based on previous internal finite element analyses carried out by SCHOTTEL, and represented the region with the highest predicted stress.

Due to ongoing maintenance work, no blades were fitted to turbines 1, 2 or 3. The instrumented blade was mounted to turbine 4/SIT 4 (starboard outer turbine, see Fig. 4) along with two other uninstrumented blades to form a complete rotor. Aside from instrumentation, the three blades were identical. The strain gauge interrogator sampled at 500 Hz, taking a reading from each of the strain gauges in sequence. This gives an effective sample rate of 167 Hz for each sensor. Other information from the platform was logged via equipment from the SURFTEC project described in Ref. [25] or through the platform's own instrumentation system [5].

Due to the weather conditions delaying the fit of the instrumented blade to the platform, the test period covered 24 h - from 15:30 on 02/03/2018 to 15:30 on 03/03/2018. This covered part of a flood tide, an ebb tide and flood tide with the rotor parked (as no overnight operations were permissible) and a single ebb tide with the instrumented turbine operating. The data from the initial partial flood tide has been disregarded for the analysis carried out here, leaving three periods to be analysed and compared, as set out in Table 1.

The local bathymetry leads to substantial flood-ebb asymmetry, with a mean flow speed of 0.26 ms^{-1} during the flood tide

Fig. 1. (L) PLAT-I on site at Connel, Scotland. Photo by SME. (R) SIT 1 raised out of the water during commissioning.

Fig. 2. Map highlighting location of the test site relative to the UK and Connel (inset). Underlying map data and original imagery OpenStreetMap contributors [23].

compared to means of 1.76 ms^{-1} and 1.65 ms^{-1} during the two recorded ebb tides. Turbulence intensity calculated over 10 min data periods was an average of 45% and 49% for the two ebb tides, with peak values of 71% and 94% respectively.

The flow speed was measured using a Nortek Vector Acoustic Doppler Velocimeter (ADV) mounted to the platform upstream of SIT 3 as shown in Fig. 4. In the configuration used, Nortek Vector has an accuracy of $\pm0.5\%$ of the recorded value ±1 mm and a quoted typical precision of up to 0.007 ms^{-1} [28]. Further examination of the recorded data and comparison to data recorded by other instrumentation during the sea acceptance trial is the subject of

future work. The coordinate system for the ADV is oriented as shown in Fig. 4, which means that the recorded x component of water flow, u_x, is usually negative. For the remainder of this document, the u_x will be inverted, such that positive values represent flow from bow to stern. The y and z components, representing flow from to the left and towards the surface respectively, are presented unchanged.

The thrust acting on the turbines was not measured directly, and is instead derived from the forces acting on stainless steel load pins used to lock each SDM into its service position. This gave a recorded value for the loads acting radially on the pin, which is then scaled
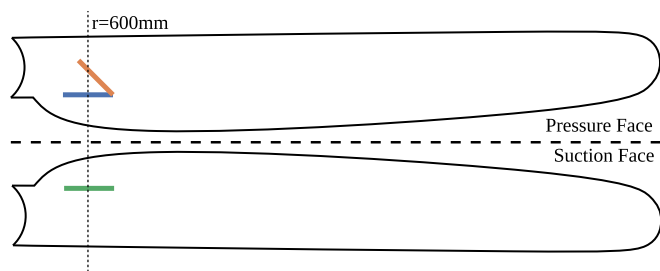
Fig. 3. Blade outline showing relative position of the two longitudinal strain gauges on the pressure and suction faces of the blade and the gauge at 45° on the pressure face to measure torsion. Not actual geometry.
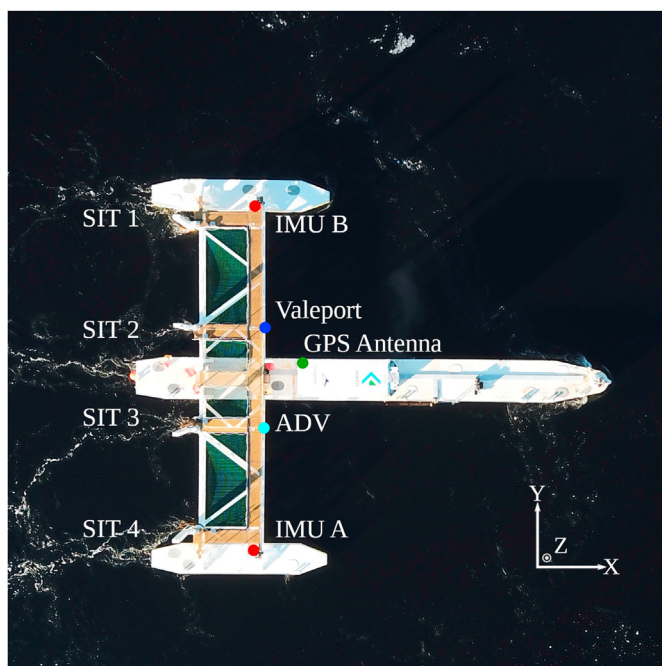

Fig. 4. Photo of PLAT-I at Connel, with key instrument positions and ADV coordinate system labelled. Original photo by SME.

Table 1
Description and times used to split the three sets of data for analysis. All dates in 2018.

Description	Period	High/Low Water
Ebb, parked	02/03 20:50 to 03/03 02:50	HW 02/03 18:26
Flood, parked	03/03 03:30 to 03/03 08:40	LW 03/03 00:39
Ebb, generating	03/03 08:40 to 03/03 15:30	HW 03/03 06:36

based on the geometry of the turbine mounting and support structure to yield an equivalent thrust at the rotor hub. This means that the thrust values used here will also include the effects of hydrodynamic loads on the support structure. The testing, development and validation of this method was carried out by Sustainable Marine Energy during a separate testing period [5]. As will be seen later, in Section 3.2, these loads are small with respect to rotor loads in both parked and generating states.

The analysis of the data has been carried out based on the principles in IEC/TS 62600-200:2013 [27], using averages over 10 min segments as mandated in the standard, with a small amount of work using 2 min segments for sensitivity analysis. For a given segment to be valid and included in further analysis, 90% of the data
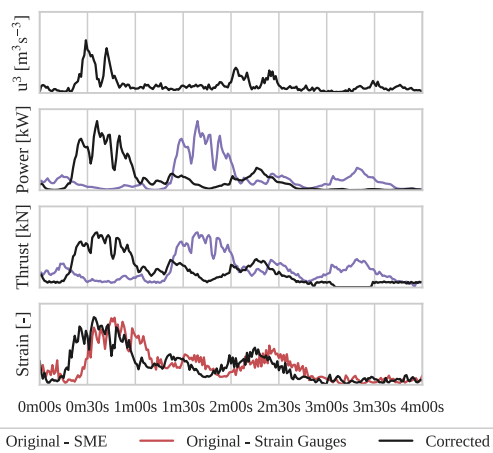

Fig. 5. 4 min sample of recorded data, showing original (purple, red) and resynchronised data (black).

points within that segment should be valid [27, 8.6]. The 90% threshold for each period was determined based on the averaging period used and the sample rate of each system. Discarding 10 min segments with less than 90% of the required number of valid samples leads to 1 segment being dropped from the strain gauge data during each of the three operating periods. The platform operational data recorded on the SME system was dropped for 1 segment during the "ebb, parked" period and 2 segments dropped during each of the flood and generating periods. Data presented here is based on results using the 10 min averaging period unless otherwise specified.

2.1. Timekeeping

The separate logging systems in use aboard PLAT-I during this test were all designed to be synchronised to UTC, either by reference to GPS or using NTP (Network Time Protocol - a standard for clock synchronisation over the internet). Despite these attempts to ensure that all devices were synchronised to a common time, some errors emerged during this analysis that required further examination.

The plots in Fig. 5 illustrate the issue, showing plots of flow speed from the ADV (recorded on the SURFTEC system), power and thrust for SIT 4 (recorded on the SME logger) and one of the recorded strains (from the strain gauge interrogator). A peak in the recorded velocity (plotted in row 1 as u^3 for ease of comparison) can be seen at the 30 s mark. Similar increases in power, thrust and strain would be expected to occur at (or nearly at) the same instant. In the uncorrected data, the corresponding increases in power and thrust (purple lines, rows 2 and 3) appear just over a minute later. The increase in recorded strain (red, row 4) is also delayed, but by approximately 10 s. By determining and correcting for the difference in recorded times for each variable, the black lines in each row are obtained - this corrected data now shows the related variations in each value occurring at the same time. Correcting the data in this manner is required when calculating quantities derived from more than one logging device, which would otherwise yield erroneous values. It should be noted that any derived quantities calculated using data solely from any individual system are not affected by the lack of synchronisation, aside from an uncertainty in the associated timestamps if these are required.

In order to correct the time difference between the different systems, variables from each system that should correlate were paired and the cross-correlation of each pair computed. Examining

where the peak in the correlation coefficients occurs allows the lag between the two systems to be determined and corrected. The cross-correlation was calculated using the fast Fourier transform (FFT) mode of the `correlate` method included in the SciPy signal processing library [29].

In the absence of a definitive UTC reference in the available data, the ADV timestamps were used as the reference clock, as both other systems could be correlated to the flow speed measured by the ADV. The correlation between u^3 and SIT 4 output power was calculated for the generating case, along with the correlation between u from the ADV and the Valeport ECM connected to the SME data logging system and the correlation between u^2 against ε_1 - the longitudinal strain gauge on the pressure face of the turbine blade.

The resulting coefficients for each of the pairs of variables identified above are shown in Fig. 6, with the correlation of the uncorrected data shown solid and lines showing the correlation of the corrected sets shown dashed to confirm that the lag has been corrected. For ease of comparison the magnitude of each curve has been normalised against its maximum value, with the resulting values shown in Table 2. There are no delay times calculated against the turbine output power, P, for the two parked periods, as the power output is zero throughout.

In addition to the time delays introduced by clock differences between systems, there will also be a spatial component to the delay times due to the physical separation between instruments and turbines. This time delay introduced by this separation is likely to be small, but dependent on flow speed. To investigate the extent of this, each case was split into individual 10 min segments. Each of these segments was then assigned to a velocity bin based on the mean velocity for that period. Each mean velocity bin covered a 0.5 ms^{-1} range, with bins covering mean velocities up to 2.5 ms^{-1}. The correlation between the flow speed recorded by the ADV and the speed recorded by the Valeport ECM was calculated for each segment, and the results of this are shown in Table 3, where positive times indicate that the timestamps recorded by the SME data logging system were later than the times recorded by the ADV and vice versa. Entries marked "N/A" indicate that there were no bins in that velocity range for that period.

There is a slight increase in the calculated delay times with increasing mean flow speeds until the $(1.0, 1.5]$ ms^{-1} bin, where the delay times shown in Table 3 peak. Although the delay times then decrease slightly with increased mean flow speed, this is small compared to the variation between individual 10 min segments.
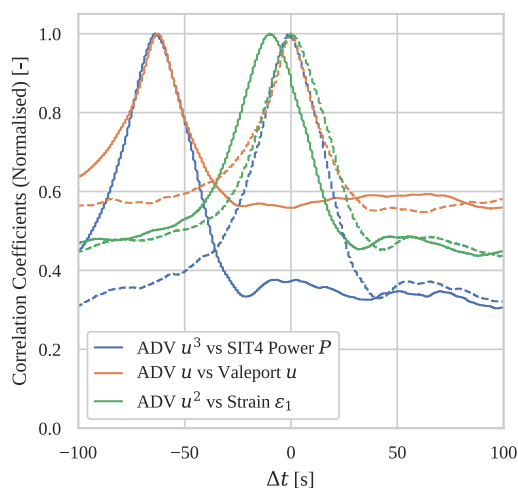
Table 2
Time differences based on cross-correlation of each pair of variables for each tide.

Pair	Ebb, Parked	Flood, Parked	Ebb, Generating
ADV vs Valeport	56.13 s	44.75 s	63.00 s
u^3 vs P	N/A	N/A	64.25 s
u^2 vs ε_1	8.63 s	− 2.50 s	10.50 s

Table 3
Time differences between platform data logging system and ADV, based on correlation between recorded ADV u_x and speed as reported by the Valeport ECM.

$\overline{V}$ [ms^{-1}]	Ebb, Parked	Flood, Parked	Ebb, Generating
(+ 0.0, + 0.5]	45.38 s	44.88 s	0.13 s
(+ 0.5, + 1.0]	54.63 s	52.13 s	58.13 s
(+ 1.0, + 1.5]	57.63 s	N/A	64.13 s
(+ 1.5, + 2.0]	56.13 s	N/A	62.63 s
(+ 2.0, + 2.5]	55.88 s	N/A	63.88 s

This is illustrated for the ebb, generating case in Fig. 7, where each point represents an individual 10 min segment, plotted against its mean flow speed. The error bars show the standard deviation of the flow speed for each bin in the horizontal direction. The vertical error bars show the standard deviation of a Gaussian fit to the peak in the correlation data to provide a broadly equivalent measure for comparison. From this, it can be seen that the variation in delay time for bins at or above 1.0 ms^{-1} shown in Table 3 is well within the variation of the individual bins.

The larger vertical error bars seen for lower velocity segments in Fig. 7 are the result of weaker correlation between the two instruments at these lower velocities such that the cross-correlation coefficients are represented by a distribution with a larger variance. At these smaller velocities, instrument noise, error, and small local flow variations will all have a proportionately larger effect on the recorded flow velocities, and these effects are likely to be independent for each instrument.

Based on this result, a single correction time has been used for each logging system for each of the three periods rather than a velocity bin based approach. The times used to resynchronise the data are the values shown in Table 2. As the SME logging system was used to record both the Valeport flow speed data and the turbine operating power, only one value is required to correct the
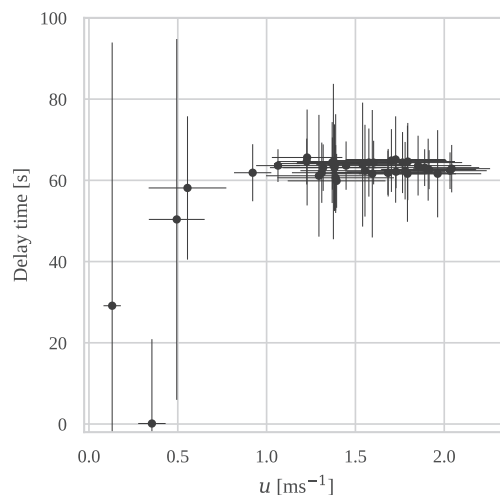

Fig. 6. Cross-correlation of three pairs of related variables for the "Ebb, Generating" case, showing original (solid) and synchronised (dashed) results.

Fig. 7. Delay time for individual 10 min segments of each velocity bin for the ebb, generating case. Bars represent an approximate standard deviation, centred on the value plotted.

timing information for the ebb, generating period. The difference in the delay times calculated using turbine power and calculated using flow speed was small (1.25 s) relative to the overall delay time (63.00 s), so the time difference calculated based on the correlation between the ADV and Valeport flow speeds was used to correct the timestamps for all three periods, to provide a consistent approach.

3. Results: timeseries

3.1. Flow conditions

The flow speed recorded at the platform for each of the three tides is shown in Fig. 8, showing the 10 min mean flow against time from high or low water for ebb and flood tides respectively. All three tides show two distinct peaks in flow speed (around the HW+4 h and HW+7 h marks), but the significantly reduced flow during the flood is clearly shown. The two ebb tides follow a very similar profile, which makes the parked ebb tide suitable for comparison to the generating case.

The turbulence intensity (TI) has been calculated from the ADV data based on the average flow speed $\overline{u}$ and the turbulent kinetic energy (TKE), k as shown in Equations (1)–(3).

$$\overline{u} = \sqrt{\overline{u_x^2} + \overline{u_y^2} + \overline{u_z^2}} \tag{1}$$

$$k = \frac{1}{2} \sum_{i=x,y,z} \left(u_i - \overline{u_i} \right)^2 \tag{2}$$

$$TI = \left| \frac{2k/3}{\overline{u}} \right| \tag{3}$$

Fig. 9 shows the turbulence intensity and turbulent kinetic energy against hours from high water for the ebb and flood tides. Both tides show a similar trend, with the turbulence in the generating case being slightly higher than the parked case after 6 h from high water. The average TI is 41% and 45% for the parked and generating cases respectively. These measurements are higher than figures generally reported at other tidal sites (e.g. 9%–17% in Ref. [7], 10%–20% in Ref. [22]), but turbulence intensities of similar value have been recorded at lower velocities as seen in Ref. [2] (averages of 10% and 25% but a range of 7%–47%). These higher values of turbulence intensity are likely to be due to the underwater overfalls at the mouth of Loch Etive and the resulting jet flow downstream of Connel Bridge during the ebb tides.

The turbulent kinetic energy for each ebb tide also correlates well, with a mean value of 0.657 J.kg^{-1} and 0.678 J.kg^{-1} for the parked and generating cases respectively, and corresponding

Fig. 9. Ten minute average Turbulence Intensity (top) and Turbulent Kinetic Energy (bottom) for recorded ebb tides, against forecast high water time. Turbulence intensity values at low flow speeds excluded.

maxima of 0.994 J.kg^{-1} and 1.06 J.kg^{-1}. The TKE distribution over time remains relatively flat through the middle of the tide (approximately HW+4 h until HW+7 h), which would indicate that the apparent peak in TI shown between HW+5.5 h and HW+6.5 h is due to the corresponding drop in velocity shown in Fig. 8 rather than a change in the energy carried as turbulent fluctuations in the flow.

3.2. Thrust and strain

Fig. 10 shows the thrust derived from the locking pin data for the two ebb tides plotted against time since forecast high water (HW). This shows both the increased load recorded for SIT 4 when parked, and the significant increase relative to the other turbines (SIT 4 was the only turbine with blades fitted). It can also be seen that SIT 1 also records a slightly higher thrust during both periods (relative to
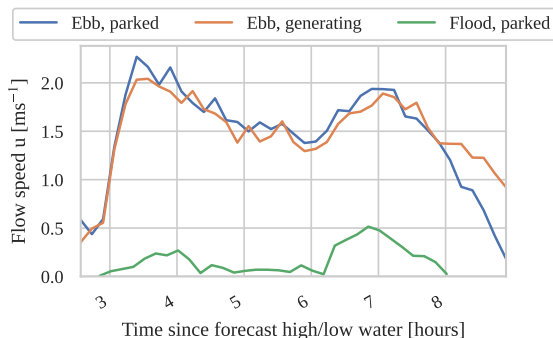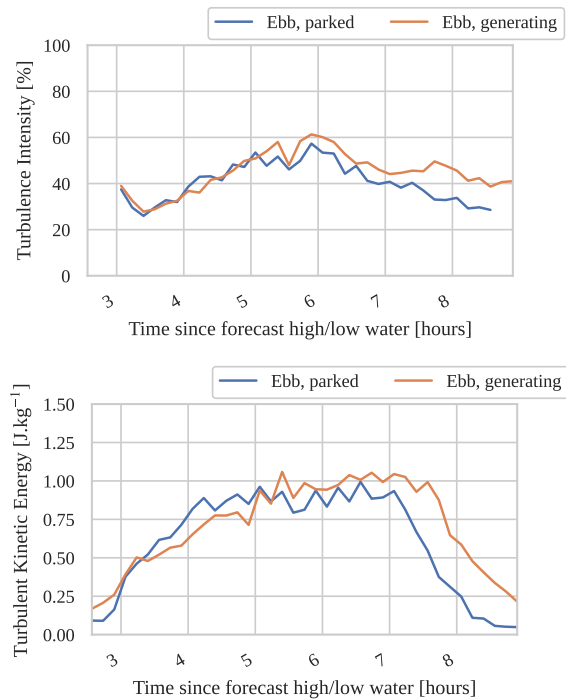

Fig. 8. Ten minute average flow speeds for the three recorded tides, against forecast high/low water time.
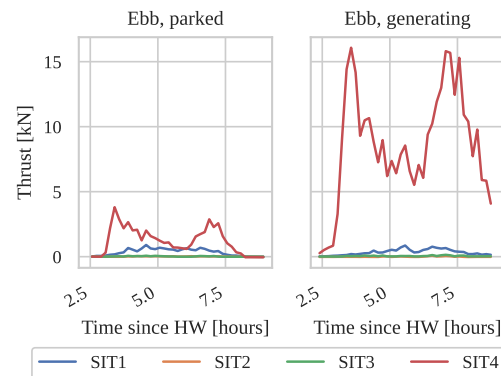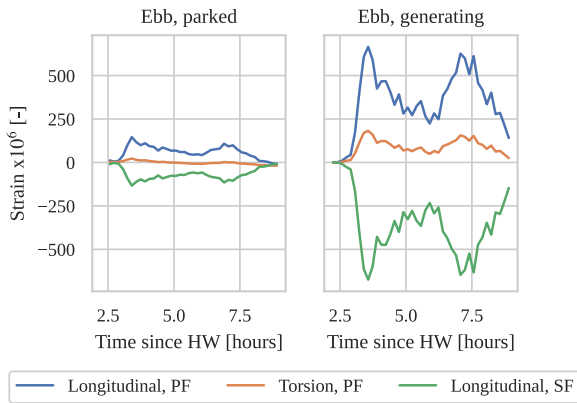

Fig. 10. Ten minute average thrust values for each SDM and turbine nacelle (with rotor for SIT 4) - under parked conditions (L) and with SIT 4 generating (R). Note that the data for SIT 2 and 3 overlap at this scale.

Fig. 11. Ten minute average strain values for the instrumented blade while parked (L) and in operation (R). PF and SF denote pressure and suction face respectively.

SITs 2 and 3), despite being in the same state. The flow conditions at Connel vary considerably depending on position within the channel, and SIT 1 lies closer to the main channel [24]. This means that for a given recorded flow speed, the flow impinging on the support structure for SIT 1 will generally be greater than the speed recorded by the ADV positioned upstream of SIT 3. This would lead to increased drag and may account for the increased apparent thrust results.

The trends visible in the average thrust data are also shown by the corresponding plots of strain recorded on the blade and shown in Fig. 11. The longitudinal strain on suction and pressure faces appears to be equal and opposite in both parked and operating conditions, as would be expected for a blade flexing flapwise (placing the pressure face in tension and the suction face into compression). The torsional strain gauge records a lower overall strain, suggesting that blade twist is smaller than blade bending, but this still correlates with the variations in flow speed (and correspondingly, both thrust and longitudinal strain).

A plot showing the correlation between thrust and strain is shown in Fig. 12. This figure shows the strain from the longitudinal strain gauge on the pressure face of the blade, plotted against the corresponding thrust recorded on SIT 4. Each blue point represents a 10 min average of each variable during the ebb tide with the turbine generating, with the solid blue line representing a linear least-squares regression fit with $R^2 = 0.963$. This is a strong correlation, and suggests that thrust values can be used to provide an indication of the strain in the blades. The points and dashed line presented in orange represent data from the same period, averaged over 2 min intervals instead of 10 min. The linear fit to 2 min data set has $R^2 = 0.968$, again showing a strong correlation between the two variables. A similar plot is obtained by comparing torque and strain, as shown in Fig. 13. In this instance, the R^2 values are 0.983 and 0.985 for the 10 min and 2 min averages respectively.

4. Results: Spectra

4.1. Flow spectra

In addition to presenting results as a timeseries, we can also examine the results in terms of their frequency spectra. The spectra shown in Figs. 14–16 have been created by splitting the input data for each operating state into 10 min intervals and creating individual spectra using a fast Fourier transform and taking the absolute value. The mean of these individual spectra were then plotted against the corresponding frequencies.

The three figures (Figs. 14–16) all show similar behaviour for the
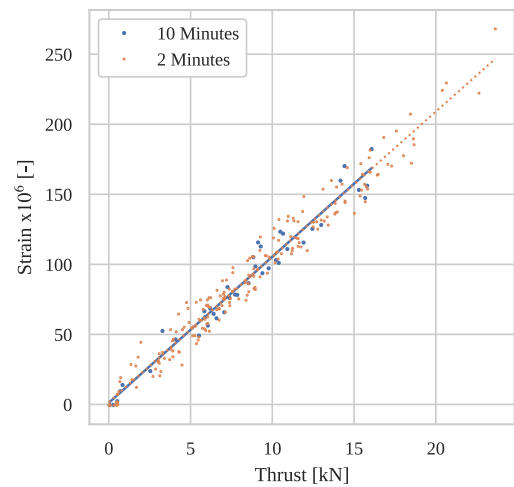
Fig. 12. Ten minute (blue) and 2 min (orange) averages of thrust and strain (from the longitudinal pressure face gauge). Lines are a linear regression fit to the data shown, with $R^2 = 0.963$ and $R^2 = 0.968$ respectively.
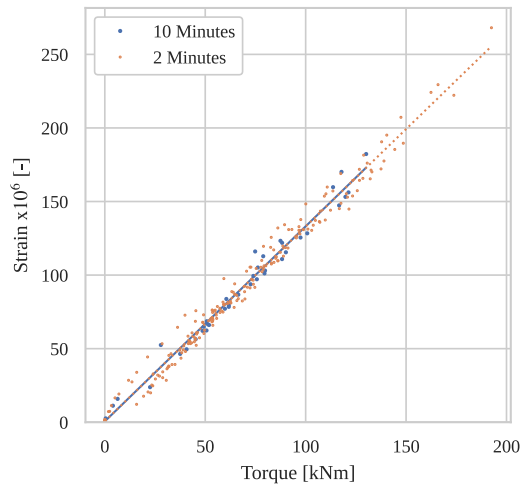
Fig. 13. Ten minute (blue) and 2 min (orange) averages of torque and strain (from the longitudinal pressure face gauge). Lines are a linear regression fit to the data shown, with $R^2 = 0.983$ and $R^2 = 0.985$ respectively.
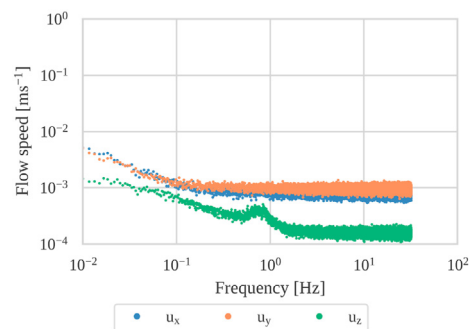
Fig. 14. Averaged velocity spectra for flood tide with blades parked. Built from individual 10 min spectra.

two horizontal velocity components, with the x component having higher values at lower frequencies (consistent with it representing the dominant flow direction due to the platform alignment). The contributions from the vertical flow component are significantly
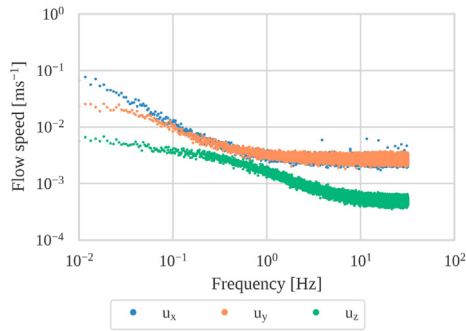
Fig. 15. Average velocity spectra for ebb tide with blades parked. Built from individual 10 min spectra.
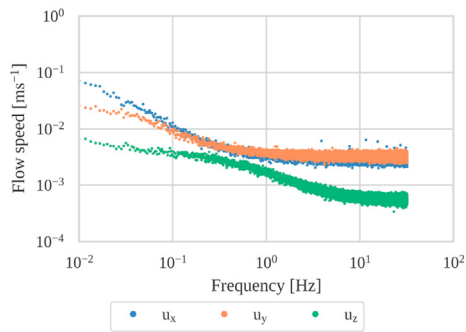

Fig. 16. Average velocity spectra for ebb tide, in operation. Built from individual 10 min spectra.

smaller than the two horizontal components, although an elevated region can be seen in the parked flood tide case (Fig. 14) just below 1 Hz. The cause of this particular contribution is not known but is probably related to the slower flow conditions on the flood tide caused by the bathymetry at the loch entrance. The general similarity between the two ebb tide cases does reiterate that conditions during the two time periods are similar enough to allow comparison of any additional loads or behaviours due to rotation of the rotors in the generating case.

4.2. Strain

Figs. 17 and 18 show the strain in the instrumented blade with the rotor parked during the ebb and flood tides respectively. As might be expected from the difference in flow speeds, the recorded strains in the flood case are lower with little variation at higher frequencies - although a very small increase in the spectra for all
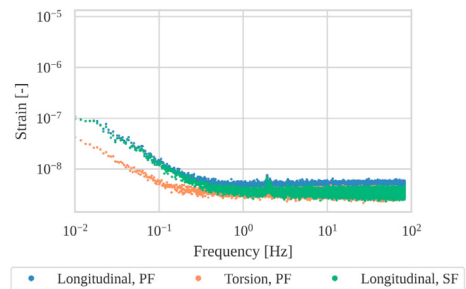

Fig. 17. Average strain spectra for flood tide with blades parked. Built from individual 10 min spectra.
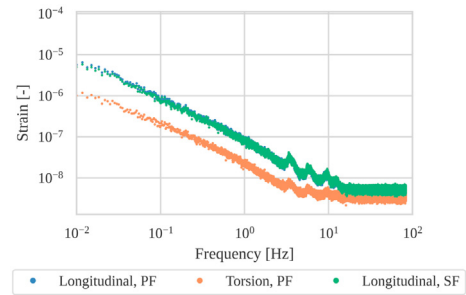

Fig. 18. Average strain spectra for ebb tide with blades parked. Built from individual 10 min spectra.

three strain gauges can be seen around 2 Hz. The ebb spectra shows generally higher values throughout, with 4 distinct peaks at approximately 3.5 Hz, 6 Hz, 9.5 Hz and 12 Hz.

Comparing the two ebb tides, it can be seen that the 4 peaks visible in the parked case (Fig. 18) are either not present or are swamped by a broadband elevation in strain between approximately 0.3 Hz and 11 Hz in the operational case (Fig. 19). The mean and maximum rotor rotation and blade pass frequencies for the periods used to produce the operational plot are shown for convenience, with the maximum rotor rotation frequency coinciding with the peak of the elevated region of the plot.

4.3. Thrust

Three averaged spectra for thrust have been produced using the same method described for strain. These results are shown in Figs. 20–22. The spectra for the parked rotor during the flood tide is relatively flat, with a small increase at low frequencies ($f < 0.1$ Hz) and a single spike centred at 2.3 Hz. This is close to, but not coincident with, the small elevation in strain seen centred at 1.9 Hz in Fig. 17.

The thrust spectra for the parked rotor in the ebb tide shown in Fig. 21 exhibits the same inner/outer turbine split as seen in the timeseries plot shown in Fig. 10. It can be seen that the split in spectra between SIT 1 (port outer turbine, without blade) and SIT 4 (starboard outer turbine, with blades) is most obvious at low frequencies, suggesting that the increased thrust measured is largely occurring at low frequencies. Conversely, the SIT 4 spectra shows slightly smaller thrust contributions at high frequencies relative to SIT 1 - possibly due to the increased mass and increased drag due to the presence of parked blades. A series of peaks can be observed in the $1\ \text{Hz} \le f \le 10\ \text{Hz}$ region. These do not directly correspond to the peaks observed in the strain spectrum in Fig. 18, but lie within a
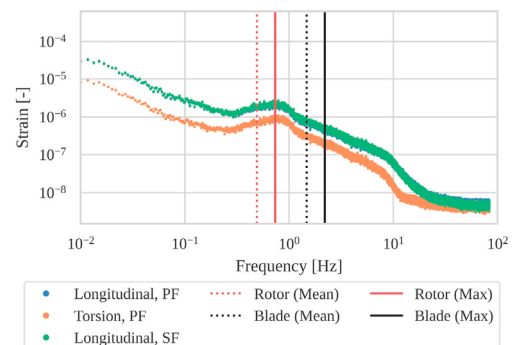

Fig. 19. Average strain spectra for ebb tide, in operation. Built from individual 10 min spectra.
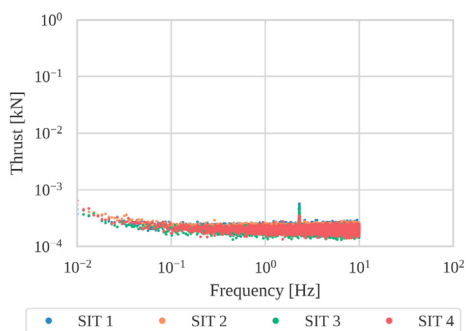
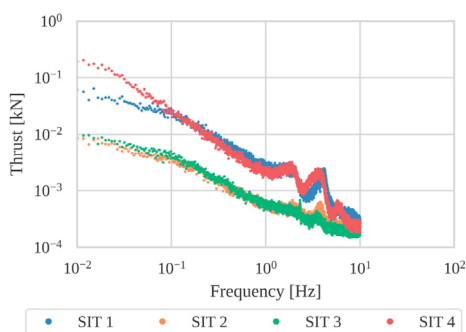**Fig. 20.** Average thrust spectra for flood tide with blades parked. Built from individual 10 min spectra.

Fig. 21. Average thrust spectra for ebb tide with blades parked. Built from individual 10 min spectra.
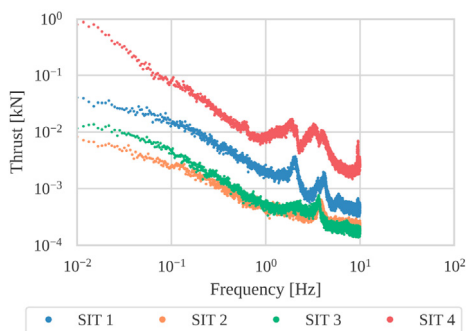

Fig. 22. Average thrust spectra for ebb tide, in operation. Built from individual 10 min spectra.

similar range. There is insufficient information available to confirm the cause of these oscillations.

During generation, SIT 4 demonstrates higher thrust across the whole frequency range shown in Fig. 22, but with a distribution that is superficially similar to the spectrum of SIT 1. Comparing the SIT 1 and SIT 4 spectra in Fig. 22, it can be seen that both have two peaks at approximately 2 Hz and 4 Hz, but these peaks are broader in the SIT 4 spectra. This broadening of the peaks could be interpreted as an effect of increased drag acting on the response of the SDM and turbine compared to SIT 1, or be due to interactions between the rotating blades and the support structure. As for the parked case, the gap between the spectra for SIT 1 and SIT 4 increases at lower frequencies, as would be expected from the higher mean thrust loads acting upon it (shown in Fig. 10).

The thrust spectra for SIT 4 for all three operating periods are plotted again in Fig. 23. This makes the relationship between the
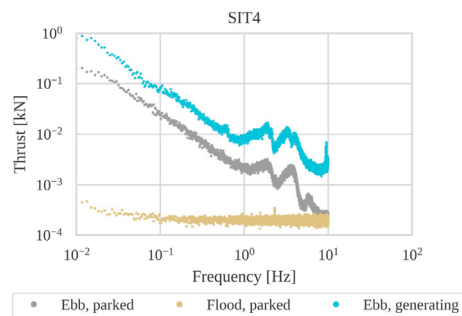

Fig. 23. Average thrust spectra for SIT 4 for all tides. Built from individual 10 min spectra.

different frequency peaks more obvious, with the more distinct peaks around 2 Hz and 4 Hz present in both ebb tides. The small feature observable at 2.3 Hz in the flood tide data is also present in the two ebb tides, but is much less distinct due to the larger and broader peaks present in the surrounding data.

The most obvious difference between the two ebb spectra for SIT 4, is the generally higher value of the spectra for the generating case - consistent with the increased load from the rotor. This increase is relatively uniform across the frequency range plotted, but there is a notable increase in high frequency contributions towards 10 Hz - note that this is the maximum resolvable frequency for this data due to the 20 Hz sample rate. Other differences between the two ebb tide spectra are the absence of a peak in the generating spectra between 5.5 Hz and 7 Hz and two small peaks in the generating spectra at 9.35 Hz and 9.55 Hz that are not seen in the results for the ebb or flood tide with the rotor parked.

4.4. Strain cycles

In order to investigate the potential fatigue implications of the loads seen on the blades, a rainflow cycle counting algorithm was applied to the data from each strain gauge. Each strain cycle can be characterised by its magnitude (shown in plots as $|\delta\varepsilon|$), and these magnitudes can be grouped into bins. The number of strain cycles is plotted against the mean cycle magnitude for each bin in Figs. 24–26 for the longitudinal gauges on the pressure and suction faces of the blade and the torsional gauge mounted on the pressure face, respectively. The algorithm used to calculate these plots is a freely available implementation of ASTM E1049-85, made public by its author at [30].

These results shown in these Figures yield the same general trends discussed above, with the generating case reflecting higher overall loads (and opportunity for larger variations) than the parked ebb flow case. This in turn shows larger load cycles than the flood parked case, for all three gauges. The difference between the two ebb tide cases for the torsional strain gauge appears to be more pronounced in the 1–100 cycle region, highlighting the effect of blade twist during generation, but with cycle strain magnitudes generally lower than for the longitudinal sensors.

5. Turbine performance

While turbine performance is not the focus of this paper, it is useful to show the power and thrust behaviour of the turbine to demonstrate that the data is representative of conditions reported elsewhere, such as in Refs. [5,24]. Fig. 27 shows the averaged values for power and thrust for 0.1 ms^{-1} velocity bins based on the 10 min average velocity recorded by the ADV using the methods described in the IEC standard [27]. As the turbine was only operating over a
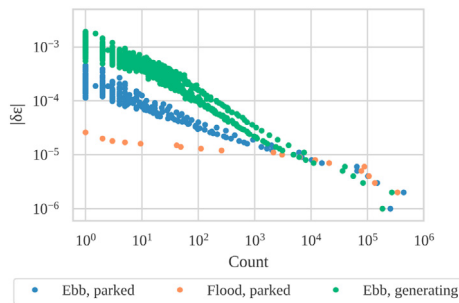
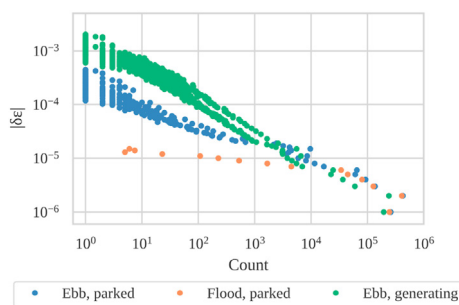**Fig. 24.** Rainflow cycle count for the longitudinal strain gauge on the pressure face of the blade.

Fig. 25. Rainflow cycle count for the longitudinal strain gauge on the suction face of the blade.
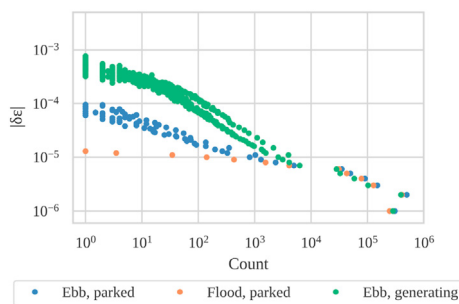

Fig. 26. Rainflow cycle count for the torsional strain gauge on the pressure face of the blade.

single tide during this particular test, the number of bins containing data for 30 min or more (the minimum specified in the standard) was limited. In order to allow the trends in the data to be more readily observed, the bins representing less than 30 min data have been included, but plotted using a different symbol (×).

Both plots (even when restricted to the standards compliant points) show behaviour consistent with results reported previously in Ref. [24], which was based on a larger dataset from the rest of the trial period. This suggests that the turbine behaviour and performance was consistent with the general testing period, and that the strain behaviour recorded here may be considered representative for similar conditions where the gauges were not fitted. Repeating the binning process with the 2 min average data does not yield any significant changes to this information, although the number of bins falling short of the IEC time requirements increases. Notably, the number of velocity bins meeting the 30 min threshold in this particular case does not change.
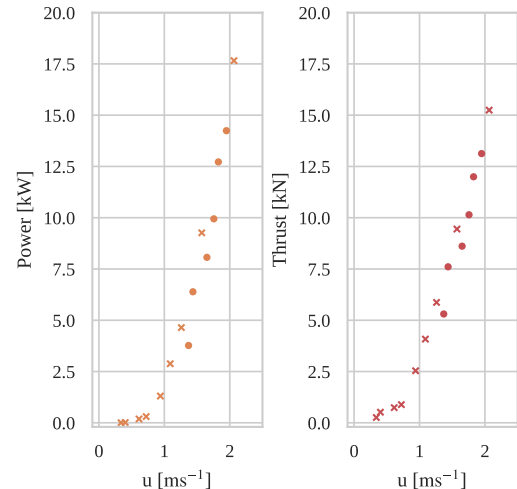

Fig. 27. Turbine output power and thrust plotted against ADV 10 min average velocity bins. Points plotted as × were based on less than 30 min data, but are included for illustration.

6. Discussion

Comparing both the timeseries and spectral information calculated from the recorded flow data show consistent flow conditions between the two available ebb tides. This is true both in terms of the averaged flow speeds and the calculated turbulent intensity, and allows the remaining data for the parked and operating states of the turbine to be compared. An simple comparison based on the 10 min averaged values shows that, as would be expected, the loads on a turbine blade and its support structure (in this case, the SDMs) during generation are substantially larger than the corresponding loads when parked. Both cases show a correlation with the measured flow speed, although the magnitude of the loads recorded for the turbines without blades showed variation across the device. This is likely due to the variation in flow speeds between the port (SIT 1) and starboard (SIT 4) side of the platform due to the local flow conditions as discussed and illustrated in Ref. [24].

Investigating the relationship between blade level loads and the loads on the turbine and supporting structure shows a strong correlation between both thrust and torque with respect to strain, as shown in Figs. 12 and 13. This suggests that variations in torque and thrust may both be used as an indicator for the blade strain when blades are uninstrumented. Given that torque is the sum of the forces acting on the blades in the rotor plane and thrust is the sum of forces acting on the blades perpendicular to the rotor plane and parallel to the rotor axis, this result is not particularly surprising. Comparison of the corresponding spectra does show that the higher frequency behaviours (at least to the limits measured here) are sufficiently different that fine scale information is not directly comparable between blade strain and either thrust or torque. In the thrust case this may be due to the forces being measured near the top of the SDM using a locking pin, meaning that the hydrodynamic drag acting on the SDM will have affected the values recorded. The drag and significantly greater inertia of the SDM and turbine (as compared to the blade alone) may well be acting to damp oscillations which will also affect both the magnitude and spectra of the recorded thrust data. This may also explain the marginally lower R^2 values applicable to the fit between thrust and strain compared to torque and strain. The correlation of both thrust and torque against strain showed no sensitivity to the choice of 10 min or 2 min averaging periods.

The rainflow cycle counting analysis performed on the recorded

strain data (Figs. 24–26) provides useful information that can be used to examine the potential fatigue limits on the blades. The largest cycle magnitudes observed for each of the three strain gauges are low frequency or singular events - although it should be noted that as the data presented here is from only a total of three tides under different operating conditions, even these singular events could be expected to occur hundreds to thousands of times per year - translating to tens of thousands of times over the design life of a turbine blade. If it can be determined that the blade and structure loads seen at higher frequencies are not a limiting factor in the lifetime of the blades then it may be possible to use the correlation between thrust and torque and blade strain to determine the frequency of the larger strain events from longer data records from other testing. Results from both lab scale tests such as [13,17] and full scale [9] tests generally show more distinct peaks associated with the blade pass and rotor rotation frequencies, which are not obviously discernible in the strain spectra shown in Fig. 19 or the thrust spectra shown in Fig. 22. Whether this was a limitation of the equipment in use or a consequence of the relatively high turbulence intensity at this site compared to the 3% and 12% values in Ref. [17], or the 12%–18% in Ref. [9], is not known.

7. Conclusions

The results presented here show the behaviour of the tidal turbine subject to highly turbulent and variable flow conditions that are associated with the test site used. Despite the presence of clock skew between different recording systems, it was possible to realign the data using a cross-correlation method, which appears to have been sufficient to allow the comparison of data between the different systems over the required averaging periods. This method should be applicable to other data recorded against independent clocks, provided that variables recorded on each system have a known/expected correlation that can be used to establish the offset between each clock.

Comparison of thrust, torque and blade level strain data shows a good correlation between these variables over the two and 10 min averaging periods that are typically used when presenting the performance of a tidal energy converter, although examination of this data in frequency space suggests that strain gauges fitted to the blades are likely to be more suitable where higher frequency load fluctuations are of interest. Whether this is a reflection of the dynamics of tidal turbines in general or an artefact of the particular instrumentation set up used here is unclear. This comparison also showed no significant difference between the results calculated using 2 min averages or the results based on 10 min averages, which may be useful information for other users of the IEC TS 62600-200 [27].

The limited amount of time available for this particular period of testing constrained the amount of data that could be recorded and analysed, and places restrictions on the ability to make longer term predictions from the data presented. However, even from a limited period the data does present additional field data that should be of interest to other developers and researchers in the area of tidal energy.

Despite the limited duration of this test. Comparison with data derived from longer term monitoring and other instruments present on the platform given in Ref. [24] suggests that the turbine behaviour during the test period presented here can be considered representative for the conditions encountered. Further work is underway comparing the velocity information from different instruments located at this turbulent and energetic site. It is useful to note that there did not appear to be any impact on the torque or output power of the turbine relative to inflow speeds during this test period due to the presence of additional instrumentation.

Declaration of competing interest

The authors declare that they have no known competing financial interests or personal relationships that could have appeared to influence the work reported in this paper.

Acknowledgements

References

[1] G.T. Scarlett, B. Sellar, T. van den Bremer, I.M. Viola, Unsteady hydrodynamics of a full-scale tidal turbine operating in large wave conditions, Renew. Energy 143 (2019) 199–213, https://doi.org/10.1016/j.renene.2019.04.123.

[2] M. Togneri, I. Masters, Micrositing variability and mean flow scaling for marine turbulence in Ramsey Sound, Journal of Ocean Engineering and Marine Energy 2 (1) (2016) 35–46, https://doi.org/10.1007/s40722-015-0036-0.

[3] M. Togneri, M. Lewis, S. Neill, I. Masters, Comparison of ADCP observations and 3D model simulations of turbulence at a tidal energy site, Renew. Energy 114 (2017) 273–282, https://doi.org/10.1016/j.renene.2017.03.061.

[4] P. Evans, A. Mason-Jones, C. Wilson, C. Wooldridge, T. O'Doherty, D. O'Doherty, Constraints on extractable power from energetic tidal straits, Renew. Energy 81 (2015) 707–722, https://doi.org/10.1016/j.renene.2015.03.085.

[5] P. Jeffcoate, N. Cresswell, Field performance testing of a floating tidal energy platform - Part 2: load performance, in: Asian Wave and Tidal Energy Conference, 2018.

[6] M. Lewis, S. Neill, P. Robins, S. Ward, M. Piano, R. Hashemi, Observations of flow characteristics at potential tidal-stream energy sites, in: Proceedings of the 11ᵗʰ European Wave and Tidal Energy Conference, 2015.

[7] B.G. Sellar, G. Wakelam, D.R.J. Sutherland, D.M. Ingram, V. Venugopal, Characterisation of tidal flows at the European marine energy centre in the absence of ocean waves, Energies 11 (1) (2018) 176, https://doi.org/10.3390/en11010176.

[8] P. Jeffcoate, R. Starzmann, B. Elsaesser, S. Scholl, S. Bischoff, Field measurements of a full scale tidal turbine, International Journal of Marine Energy 12 (2015) 3–20, https://doi.org/10.1016/j.ijome.2015.04.002.

[9] M. Harrold, P. Ouro, Rotor loading characteristics of a full-scale tidal turbine, Energies 12 (6) (2019) 1035, https://doi.org/10.3390/en12061035.

[10] H.J. Sutherland, On the fatigue analysis of wind turbines, Tech. Rep. SAND99-0089, Sandia National Labs., Albuquerque, NM (US), Sandia National Labs., Livermore, CA (US), Jun. 1999, https://doi.org/10.2172/9460.

[11] F. Elasha, D. Mba, M. Togneri, I. Masters, J.A. Teixeira, A hybrid prognostic methodology for tidal turbine gearboxes, Renew. Energy 114 (2017) 1051–1061, https://doi.org/10.1016/j.renene.2017.07.093.

[12] I.A. Milne, A.H. Day, R.N. Sharma, R.G.J. Flay, Blade loading on tidal turbines for uniform unsteady flow, Renew. Energy 77 (2015) 338–350, https://doi.org/10.1016/j.renene.2014.12.028.

[13] B. Gaurier, P. Davies, A. Deuff, G. Germain, Flume tank characterization of marine current turbine blade behaviour under current and wave loading, Renew. Energy 59 (2013) 1–12, https://doi.org/10.1016/j.renene.2013.02.026.

[14] G.S. Payne, T. Stallard, R. Martinez, Design and manufacture of a bed supported tidal turbine model for blade and shaft load measurement in turbulent flow and waves, Renew. Energy 107 (2017) 312–326, https://doi.org/10.1016/j.renene.2017.01.068.

[15] N. Barltrop, K.S. Varyani, A. Grant, D. Clelland, X. Pham, Wave-current interactions in marine current turbines, Proc. IME M J. Eng. Marit. Environ. 220 (4) (2006) 195–203, https://doi.org/10.1243/14750902JEME45.

[16] O. de la Torre, D. Moore, D. Gavigan, J. Goggins, Accelerated life testing study of a novel tidal turbine blade attachment, Int. J. Fatig. 114 (2018) 226–237, https://doi.org/10.1016/j.ijfatigue.2018.05.029.

[17] G.S. Payne, T. Stallard, R. Martinez, T. Bruce, Variation of loads on a three-bladed horizontal axis tidal turbine with frequency and blade position, J. Fluid Struct. 83 (2018) 156–170, https://doi.org/10.1016/j.jfluidstructs.2018.08.010.

[18] M. Allmark, R. Ellis, C. Lloyd, S. Ordonez-Sanchez, K. Johannesen, C. Byrne, C. Johnstone, T. O'Doherty, A. Mason-Jones, The development, design and characterisation of a scale model Horizontal Axis Tidal Turbine for dynamic load quantification, Renew. Energy 156 (2020) 913–930, https://doi.org/10.1016/j.renene.2020.04.060.

[19] F. Maganga, G. Germain, J. King, G. Pinon, E. Rivoalen, Experimental characterisation of flow effects on marine current turbine behaviour and on its wake properties, IET Renew. Power Gener. 4 (6) (2010) 498–509, https://doi.org/10.1049/iet-rpg.2009.0205.

[20] I.A. Milne, R.N. Sharma, R.G.J. Flay, S. Bickerton, Characteristics of the turbulence in the flow at a tidal stream power site, Phil. Trans. Math. Phys. Eng. Sci. 371 (2013) (1985) 20120196, https://doi.org/10.1098/rsta.2012.0196.

[21] L. Cea, J. Puertas, L. Pena, Velocity measurements on highly turbulent free surface flow using, ADV, Experiments in Fluids 42 (3) (2007) 333–348, https://doi.org/10.1007/s00348-006-0237-3.

[22] K. McCaffrey, B. Fox-Kemper, P.E. Hamlington, J. Thomson, Characterization of turbulence anisotropy, coherence, and intermittency at a prospective tidal energy site: observational data analysis, Renew. Energy 76 (2015) 441−453, https://doi.org/10.1016/j.renene.2014.11.063.

[23] Openstreetmap Contributors, https://www.openstreetmap.org/.

[24] R. Starzmann, I. Goebel, P. Jeffcoate, Field performance testing of a floating tidal energy platform - Part 1: power performance, in: Asian Wave and Tidal Energy Conference, 2018.

[25] T. Lake, A.J. Williams, I. Masters, Motion tracking of a free-yawing floating tidal stream turbine platform, in: Proceedings of the 13th European Wave and Tidal Energy Conference, Naples, Italy, 2019.

[26] K. Greening, A. Hodgson, Atmospheric analysis of the cold late February and early March 2018 over the UK, Weather 74 (3) (2019) 79−85, https://doi.org/10.1002/wea.3467.

[27] Part 200: Electricity Producing Tidal Energy Converters - Power Performance Assessment, Standard IEC TS 62600-200, International Electrotechnical Commission, May 2013.

[28] Nortek, Nortek | Vector - 300 m, last accessed 06/01/2021 18:04:08. URL https://www.nortekgroup.com/products/vector-300-m.

[29] P. Virtanen, R. Gommers, T.E. Oliphant, M. Haberland, T. Reddy, D. Cournapeau, E. Burovski, P. Peterson, W. Weckesser, J. Bright, S.J. van der Walt, M. Brett, J. Wilson, K.J. Millman, N. Mayorov, A.R.J. Nelson, E. Jones, R. Kern, E. Larson, C.J. Carey, İ. Polat, Y. Feng, E.W. Moore, J. VanderPlas, D. Laxalde, J. Perktold, R. Cimrman, I. Henriksen, E.A. Quintero, C.R. Harris, A.M. Archibald, A.H. Ribeiro, F. Pedregosa, P. van Mulbregt, SciPy 1.0: fundamental algorithms for scientific computing in Python, Nat. Methods 17 (3) (2020) 261−272, https://doi.org/10.1038/s41592-019-0686-2.

[30] P. Janiszewski, Implementation of the Rainflow-Counting Algorythm in Python, Dec. 2019. https://github.com/iamlikeme/rainflow. (Accessed 13 August 2020).